ROYAL SOCIETY
OF CHEMISTRY

PAPER

Nanostructure formation mechanism and ion diffusion in iron–titanium composite materials with chemical looping redox reactions

Lang Qin,†[a] Zhuo Cheng,†[a] Jonathan A. Fan,[b] David Kopechek,[a] Dikai Xu,[a] Niranjani Deshpande[a] and Liang-Shih Fan*[a]

Iron oxide composites are enabling materials in energy conversion systems including chemical looping and photocatalysis. Extensive earlier experimental findings indicate that inert oxides such as titanium oxide can greatly improve the reactivity of iron oxide over multiple redox cycles. Knowledge on the evolution of the nanoscale morphology of the Fe–Ti materials during the oxidation and reduction is thus of considerable importance. It is also of interest to the fundamental understanding of the ion diffusion mechanism in the reaction processes. In this study, Fe–Ti composite microparticles undergoing cycles of oxidation and reduction are examined at the nano-scale, and the interfacial characteristics of the iron titanium oxides within the composites are probed. Nanobelts are observed to simultaneously form on the microparticle surface during the oxidation at 700 °C, while microblades are found at 900 °C. Additionally, unlike pure iron microparticles that become dense on surface due to sintering effect, Fe–Ti microparticles are transformed into porous particles after redox cycles. The atomistic thermodynamics methods and density functional theory calculations are carried out to investigate the ionic diffusion and vacancy formation during the oxidation and reduction process. A number of surface configurations are considered, and the Ti–Ti–O– terminated surface is computed to the most stable surface structure at experimental conditions. It was found that in oxidation processes, surface Ti atoms are more favorable for oxygen adsorption and dissociation than Fe atoms. The energy barrier of Fe ion diffusion towards the surface, on the other hand, is lower than Ti ion diffusion, which contributes to the Fe_2O_3-dominant nanobelt formation. The volume change due to high temperature associated with the solid state transformation at the $Fe_2O_3/FeTiO_3$ interface produces compressive stresses, which stimulate Fe_2O_3 nanobelt growth to accompany the interface reaction. Also, as the vacancy formation energy of $FeTiO_3$ is lower than Fe_2O_3 in the reduction process, it indicates that it is easier for a $FeTiO_3$ surface to form vacancy defects, thereby enhancing the porous surface structure formation and O_2 diffusivity. The good agreements between experiments and DFT calculations further substantiate nanostructure formation mechanism in redox reactions of iron titanium composite materials.

Introduction

The clean energy industry requires highly efficient materials with low cost and high performance and durability. Metal oxides are among the most versatile candidates, exhibiting a wide range of promising physical and chemical properties. In particular, composites of metal oxides are enabling materials for operation in many energy conversion systems. For example, ZnO nanowires enable faster electron injection in dye-sensitized solar cells;[1] ionic conductors consisting of ZrO_2 doped with

Y_2O_3 (YSZ) are commonly used as electrolyte materials in solid oxide fuel cells (SOFC);[2] perovskite ABO_3 exhibit excellent properties in photovoltaics, light emitting diodes and photocatalytic conversion;[3] and Fe–Ti based oxide composites have been successfully demonstrated to recycle over thousands of times in chemical looping systems.[4] The ionic and electrical conductivity, optical properties and chemical properties of metal oxides and their composites are intrinsically determined by their crystal structures, electron structures and morphologies. Catalyst-free thermal oxidation offers various operational advantages in synthesizing metal oxide nanomaterials including continuous production, self-purification, and scalability.[5,6] In particular, the growth of nanobelts that possess a rectangular cross section and a uniform structure using catalyst-free thermal oxidation can be promising in producing the building blocks for integrated electronic and photonic

[a]Department of Chemical and Biomolecular Engineering, The Ohio State University, 140 West 19th Ave, Columbus, OH 43210, USA. E-mail: fan.1@osu.edu

[b]Department of Electrical Engineering, Ginzton Laboratory, Spilker Engineering and Applied Sciences, Stanford University, 348 Via Pueblo Mall, Stanford, CA 94305, USA

† These authors contributed equally to this work.

circuits.[7,8] In many energy conversion applications of metal oxides, a key step involves the transport of charged particles including electrons, ions and other defects. Consequently, it is critical to understand the diffusion of point defects and to control the morphology of these materials in processes associated with the material growth as in the high temperature oxidation of metals to form metal oxides, and their associated reduction reactions. Metal oxides, their composites, and the reduction and oxidation reactions conducted in this study are of special relevance for chemical looping systems and photocatalysis.

For many applications involving electron and ion transport, oxide material performance can be enhanced by their nanoscale processing.[9,10] The ion diffusion in metal oxide materials plays a significant role in their reduction and oxidation reactions that are accompanied with morphological and structural changes. Chemical looping is regarded as a cost effective technique[11,12] for clean conversion of carbonaceous fuels along with CO_2 capture. A chemical looping system converts carbonaceous fuels to energy using metal oxide based oxygen carriers and can be operated under various modes.[13] In the chemical looping gasification (CLG) mode, hydrogen and heat are co-generated, while the oxygen carriers circulate among three reactors: a reducer, an oxidizer, and a combustor. In the chemical looping combustion (CLC) mode, the oxidizer is excluded and the oxygen carriers are completely oxidized only in the combustor, thus producing only heat. The chemical looping oxygen uncoupling (CLOU) process mode is based on CLC with metal oxides releasing gaseous oxygen (O_2) to convert carbonaceous fuels. In all of these chemical looping modes of operation, the diffusion of metal ions, oxygen ions, and oxygen vacancies dictates the redox reactivity and recyclability of the metal oxide oxygen carriers.[14]

In an earlier work, active metal oxide systems including Fe_2O_3 were examined under cyclic redox conditions.[6] Upon oxidation, nanopores and Fe_2O_3 nanowires were observed at the surface of the oxidized Fe_2O_3 microparticles. Upon reduction by H_2 or multiple redox cycles thereafter, the nanowires and nanopores disappeared at the surface and micropores were formed on the microparticles. These phenomena were associated with ion diffusion and volume expansion. Active metal oxide systems include individual or mixed oxides of iron, nickel, manganese, copper, and cobalt, as well as oxides of alkaline earth metals such as calcium. These systems play an important role as active oxygen carrier materials in CLC, CLG, and CLOU[15–18] because of their capability for being fully reduced and oxidized for multiple cycles. However, high temperature sintering hinders the direct application of active systems due to substantial surface morphology change and porosity decreases, which result in less active surface area. Inert metal oxides usually contain one or more oxides that have a low reaction rate with reducing or oxidizing gases, e.g., rutile, corundum, perovskite or spinel structures. The system Tammann temperature of Fe_2O_3 is increased by ~120 K by the addition of TiO_2 support, which may slightly decrease the system reactivity during the redox reactions. Nevertheless, proper addition of inert metal oxides is believed to increase the system ionic conductivity,

which promotes the inward and outward diffusion of oxygen ions and thus promotes the reaction rates.[19] However, in active/inert systems, solid state reactions due to the Kirkendall effect[6] and gas–solid reactions in oxidation/reduction processes are associated with atom rearrangement and phase changes in the oxides. This behavior complicates the mechanism study in active/inert systems and is rarely discussed in previous work.[19] A comprehensive understanding of the ion diffusion in metal oxide composites is essential to a better design and application for chemical looping systems. In this work, the morphological and phase study is combined with atomic modeling to illustrate the phenomena of the surface and internal evolution of the active/inert systems in redox reactions. Crystalline Fe–Ti microparticles are used as a model system in this work. The effects induced by ion diffusion occurring deep within the microparticle core are probed by using focused ion beam nanomachining for visualizing the composition and morphology of individual microparticle cross-sections, and by using atomistic thermodynamics combined density functional theory calculation for revealing the nanostructure formation mechanism in the redox process.

Methods

Experimental

Fe–Ti (Fe60/Ti40) powders (99% + purity) with 325 mesh were purchased from Goodfellow USA. The average particle size was 30 μm based on the Scanning Electron Microscopy (SEM) analysis. The powders were washed with acetone three times and pre-treated under a 200 mL min^{-1} flow of gas consisting of 50% H_2 and 50% N_2 for 60 minutes at 100 °C prior to reactivity tests. Approximately 0.1 g powder samples were mounted in a quartz crucible and run through either one oxidation step or between one and five oxidation–reduction cycles at 700 °C and 900 °C using a Setaram SETSYS Evolution Thermogravimetric Analyzer (TGA). Oxidation was performed using a 200 mL min^{-1} flow of gas consisting of 50% air balanced with N_2. The reduction step used a 200 mL min^{-1} flow of gas containing 50% H_2 balanced with N_2. The oxidation and reduction steps lasted for 30 minutes each and were alternated with an intermediate 10 minute flushing step using N_2 at 100 mL min^{-1}. All samples were analyzed using a Rigaku SmartLab X-ray Diffractometer (XRD) with eliminated fluorescence. Scans were run from 30–80 degrees at a rate of 1 degree per minute with an accelerating voltage and filament current of 40 kV and 44 mA, respectively. All of the XRD spectra were analyzed using PDXL software and identified with the JCPDF database.

Scanning Electron Microscopy (SEM) samples were examined with a 20 kV and 43 pA electron beam. Secondary electron images were obtained with a working distance of 4.1 mm. Energy dispersive X-ray spectra and 2-D material mapping were obtained using Oxford Energy Dispersive X-ray Spectrometry (EDS) at an accelerating voltage of 20 kV. Particle cross-sections were prepared using the FEI Helios NanoLab600 DualBeam system, where samples were tilted at 52° and adjusted at the eucentric height for dual beam imaging. Ga ions were generated at an accelerating voltage of 30 kV. A regular cross section was

first performed at an ion beam of 2.8 nA, followed by a cleaning cross section milling at 0.28 nA.

Computational

In redox reactions of Fe–Ti composite materials, Fe and Ti are first oxidized into metal oxides. It is important to examine the atomic structure of the particle surface and ion diffusion in the redox reactions in order to understand the mechanism of nanostructure formation. The first-principle calculations were performed within the framework of density functional theory (DFT), using the Vienna Ab Initio Simulation Package (VASP).[20–22] The generalized gradient approximation of Perdew, Burke and Ernzerhof[23] was used to represent the exchange–correlation energy. The projector-augmented wave (PAW) method,[24,25] with a 400 eV energy cutoff, was used to describe the wavefunctions of the atomic cores. The tetrahedron method with Blöchl corrections[26] was used to set the partial occupancies for the orbitals. While several k-point mesh sizes (e.g., $4 \times 4 \times 1$ up to $13 \times 13 \times 4$) were considered, ultimately the $6 \times 6 \times 1$ Monkhorst–Pack k-point mesh was used for surface calculations to give results that were sufficiently converged within 1×10^{-5} eV, using the conjugate gradient method. Fe–Ti composite materials contain two distinct transition-metal cations that allow partially occupied d shells (for example, for $FeTiO_3$, it has two different cation charge orderings $Fe^{2+}Ti^{4+}$ and $Fe^{3+}Ti^{3+}$), being consistent with O^{2-} anions. The Local Density Approximation (LDA) and the Generalized Gradient Approximation (GGA) fail to correctly treat d orbitals due to unphysical self-interaction. Therefore, the Hubbard U parameter was employed within the GGA + U approach.[27,28] The Hubbard U term acts as an onsite Coulombic interaction to properly localize the electrons in these states. $U = 5$ eV was used for Fe ions to explore the correlation effects in 3d orbitals, whereas $U = 1$ eV was used for Ti ions due to the nearly empty 3d orbitals. The calculated lattice parameters for $FeTiO_3$ are $a = b = 5.103$ Å and $c = 14.121$ Å, which is in good agreement with the experiment data, in which $a = b = 5.087$ Å and $c = 14.083$ Å.[29]

For ionic diffusion and reaction barrier calculations, the climbing-image nudged elastic band (CI-NEB) method was used.[30,31] This method enabled the stationary points to be mapped out along the minimum energy paths and identify transition states for each of the diffusion processes. Because these paths were directed by force projection, the energy was not necessarily consistent with the force being optimized; thus, the force-based optimizer was chosen to ensure the convergence of the nudged elastic band algorithm.

Results and discussion

The initial Fe–Ti microparticles were subjected to XRD analysis, and were found to be composed of Fe (JCPDF 87-0721) and Ti_6O (JCPDF 72-1807). Here, Ti_6O can be treated as slightly oxidized Ti in this work. The XRD spectrum of the initial microparticles can be seen in Fig. 1(a).

The surface and cross sectional SEM images (Fig. 2(a and b)) of a typical Fe–Ti microparticle suggest that the microparticles
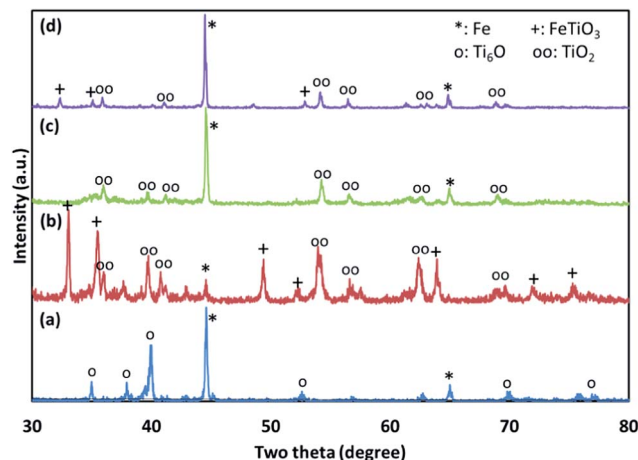

Fig. 1 XRD spectra of Fe–Ti particle. (a) initial (b) after oxidation (c) after one oxidation–reduction cycle (d) after five oxidation–reduction cycles at 700 °C.

are dense with few voids (Fig. 2(c)). In addition, the image of the EDS mapping implies that the two phases are non-homogeneously mixed (Fig. 2(d)) with an iron-rich part separated from a titanium-rich part.

Thermal oxidation and nanostructure formation in Fe–Ti microparticles

The Fe–Ti microparticles were subjected to oxidation at two different temperatures of 700 °C and 900 °C. Their morphological and phase characterization, the atomic structure evolution, and oxygen adsorption–dissociation and the ionic diffusion as a driving mechanism for the nanostructure growth are discussed below.
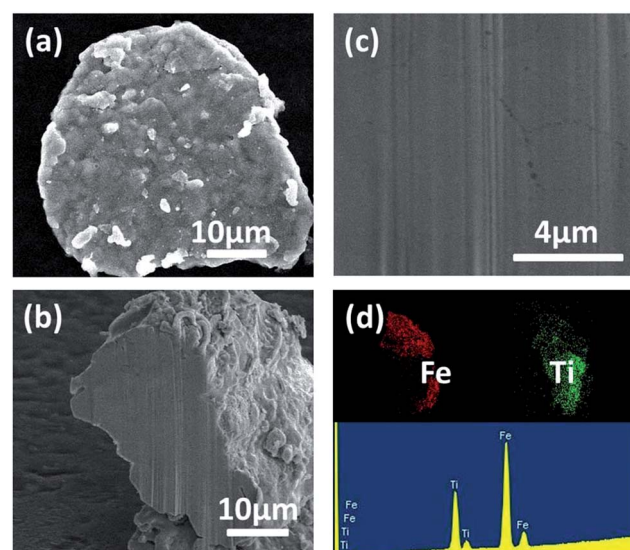

Fig. 2 Characterization of Fe–Ti particle. (a) SEM image of top surface of initial iron titanium particle; (b) SEM image of cross-section of the same particle after oxidation; (c) cross section at higher magnification (d) EDS mapping of Fe and Ti from (b).

11304 | J. Mater. Chem. A, 2015, 3, 11302–11312

This journal is © The Royal Society of Chemistry 2015

Morphological and structural characterization of oxidized Fe–Ti microparticles

After the oxidation, the phases are converted to $FeTiO_3$ (JCPDF 75-1212) and TiO_2 (JCPDF 86-147). The XRD spectrum of the microparticles oxidized at 700 °C is seen in Fig. 1(b). Here, the titanium oxide is in the rutile structure which creates more effective pathways for oxygen diffusion than the anatase structure.[32] During the thermal oxidation, nanobelts that contain Fe, Ti, and O are found to protrude from the surface of oxide microparticles, as shown in Fig. 3(a) and (b).

In contrast to other nanowire formation during the thermal oxidation,[33–37] measurements based on SEM images show that the nanobelts have widths ranging from 150 to 200 nm and width/thickness ratios from 5 to 10. Each of the nanobelts has a triangular tip (Fig. 3(b)), suggesting an anisotropic growth in the initial stage.[38] The detailed growth mechanism of these nanobelts is discussed further in section *Nanostructure growth and ion diffusion*. In general, thermal oxidation causes volume expansion that accommodates inward diffusion of oxygen, and this volume expansion becomes the driving force for nanostructure growth. The porous center of the microparticles is developed due to the outward diffusion of Fe and Ti atoms during the oxidation. Ti is oxidized to TiO_2 and participates in a solid state reaction with iron oxide to form ilmenite phase $FeTiO_3$.

Upon oxidation of the microparticles at 900 °C, a phase conversion to $FeTiO_3$ and TiO_2 takes place, similar to that observed at 700 °C. This is confirmed in the XRD spectrum in Fig. 4(a).

Unlike the nanobelts found on the surface of samples treated at 700 °C, microblades were observed on the surface of the microparticles oxidized at 900 °C (Fig. 5). The microblades were noted to have a round top with a tip width of 200 nm and the
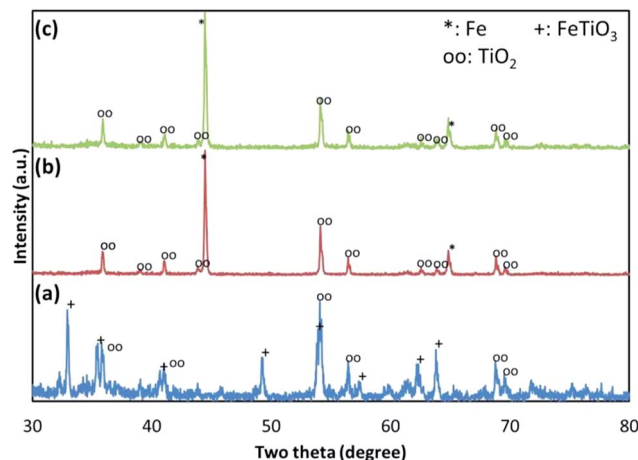

Fig. 4 XRD spectra of iron titanium particle treated at 900 °C. (a) after oxidation (b) after one oxidation–reduction cycle (c) after five oxidation–reduction cycles.

width gradually increases from top to bottom with a halfway width of 2 μm. The microblades contained Fe, Ti and O (Fig. 5(d) bottom) which is identical to the nanobelts formed at 700 °C.

Clearly, higher temperature leads to larger nanostructure growth. Noticing that the tip width is the same as the nanobelts treated at 700 °C, the growth can be explained by the sintering effect as follows. At 900 °C the growth rate of nanobelts is expected to be faster than that at 700 °C. Consequently, once the nanobelts reach their maximum length during oxidation, they start to merge into each other after continuous lateral growth. Evidence of this fact is seen in the Fig. 5(b) (circled). A microblade forms with non-uniform length, which is caused by the differences in the maximum nanobelt lengths.
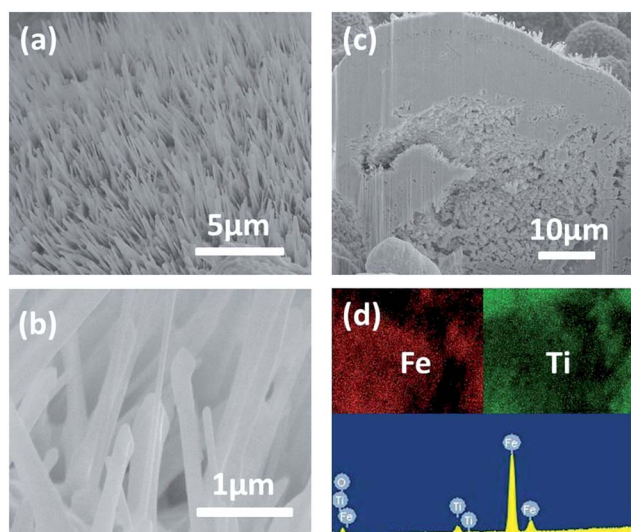

Fig. 3 Characterization of the oxidized microparticles at 700 °C. SEM image of the surface of the microparticles at (a) lower magnification and (b) higher magnification. (c) SEM image of cross-section of one microparticle. (d) Top: EDS mapping of Fe and Ti from (c); bottom: EDS spectrum of the cross-section.
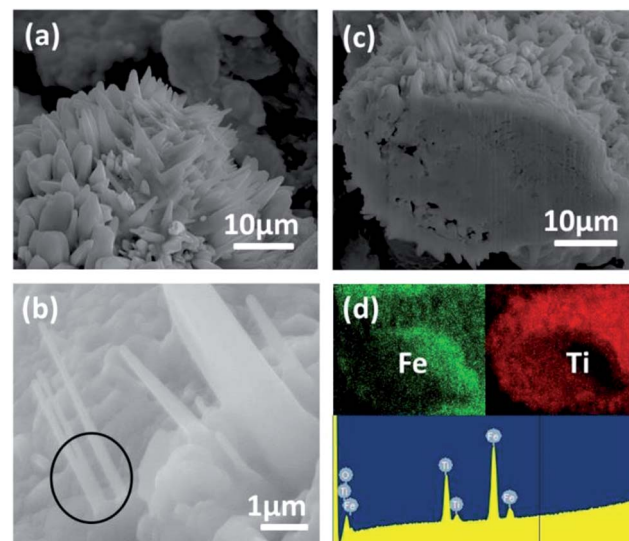

Fig. 5 Characterization of the oxidized microparticles at 900 °C. SEM image of the surface of the microparticles at (a) lower magnification and (b) higher magnification. (c) Cross-section of the SEM of one microparticle. (d) Top: EDS mapping of Fe and Ti from (c); bottom: EDS spectrum of the cross-section.

Computation of surface atomic structure during thermal oxidation. As seen in XRD spectrum (Fig. 1(b)), after oxidation at 700 °C the Fe and Ti_6O phases are converted to $FeTiO_3$ and TiO_2. Although TiO_2 has been well studied, there are only a few studies on the structure of $FeTiO_3$ surfaces. Wilson *et al.*[39] reported that $FeTiO_3$ has a hexagonal close-packed oxygen lattice and its metal atoms occupy two-thirds of the available octahedral sites. Fellows *et al.*[40] demonstrated that clean $FeTiO_3$ (0001) surfaces are stable and can relax in an unreconstructed termination. Along the (0001) direction, $FeTiO_3$ can be regarded as a stack of layers comprised of Fe, Ti and O. From experimentation alone, it is difficult to probe the $FeTiO_3$ (0001) surface termination which can significantly affect surface reaction and inward/outward diffusion. Computer simulations were therefore employed as an ideal tool to describe and analyze the surface atomic structure.

$FeTiO_3$ bulk is based on the higher symmetry corundum structure (space group $R\bar{3}c$). The metal atoms all lie on threefold axes parallel to c axis, forming the sequence of face-shared pairs of octahedra alternating with vacant octahedral sites in the middle. To model the surface slab, the $FeTiO_3$ bulk is cleaved along the (0001) surface. A 15 Å thick vacuum layer was used to separate the surfaces and their images. The use of the periodic models avoids the introduction of edge effects and allows for a more accurate description of surface relaxation. The layers can be described as the repeat of –O–Fe(1)–Fe(2)–O–Ti(1)–Ti(2)– ordering as shown in Fig. 6. A semi-infinite slab was used to represent the $FeTiO_3$ (0001) surface. Depending on the cleavage position, six possible terminations can be built:

(a) O–Fe(1)–Fe(2)–
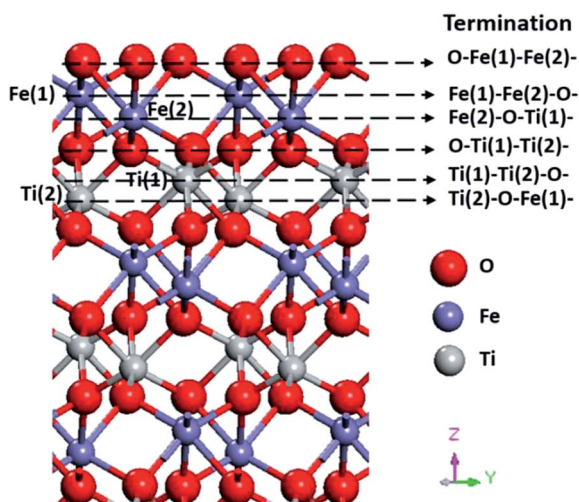
(b) Fe(1)–Fe(2)–O–

(c) Fe(2)–O–Ti(1)–

(d) O–Ti(1)–Ti(2)–

(e) Ti(1)–Ti(2)–O–

(f) Ti(2)–O–Fe(1)–

Because the oxidation and reduction of Fe–Ti particles occur in a high temperature process, DFT calculations were combined with statistical mechanics and thermodynamics by entering DFT total energies into the calculations of the Gibbs free energy $G(T, p)$ to compare the stability of the various surface terminations in experimental conditions.

The $FeTiO_3$ (0001) surface energy γ at temperature T and pressure p can be written as:

$$\gamma(T,p) = \frac{1}{A}[G(T,p) - N_{Fe}\mu_{Fe} - N_{Ti}\mu_{Ti} - N_O\mu_O] \quad (1)$$

where μ_{Fe}, μ_{Ti} and μ_O are the chemical potentials of Fe, Ti, and O, respectively, and N_{Fe}, N_{Ti} and N_O are the number of Fe atoms, Ti atoms and O atoms, respectively. A is surface area, and G is given by:

$$G(T, p) = E_{DFT} - TS + PV \quad (2)$$

For a solid slab system, the vibrational entropy S_{vib} is the main contribution. It can be directly obtained from the vibrational partition function, using the DFT-estimated frequencies v_i:

$$S_{vib} = \sum_{n=1}^{N}\left[\frac{hv_i}{T}\frac{X_i}{1-X_i} - k_B\ln(1 - X_i)\right] \quad (3)$$

where $X_i = \exp(-hv_i/k_BT)$.

Because $\mu_{FeTiO_3} = \mu_{Fe} + \mu_{Ti} + 3\mu_O$ and $N_{Fe} = N_{Ti}$ in this slab, the surface energy equation can be simplified to:

$$\gamma(T,p) = \frac{1}{A}\left[G(T,p) - \left(N_{Fe}\mu_{FeTiO_3} - 3N_{Fe}\mu_O + N_O\mu_O\right)\right] \quad (4)$$

However, if there are vacancies in the slab, N_{Fe} will be different from N_{Ti}. In this case, Fe_2O_3 can be used as the chemical potential reference for Fe as given by:

$$\mu_{Fe_2O_3} = 2\mu_{Fe} + 3\mu_O \quad (5)$$

The chemical potential of Ti can then be calculated from the μ_{FeTiO_3} expression:

$$\mu_{Ti} = \mu_{FeTiO_3} - 3\mu_O - \left(\frac{\mu_{Fe_2O_3} - 3\mu_O}{2}\right) \quad (6)$$

which gives a surface energy at T and p according to:

$$\gamma(T,p) = \frac{1}{A}\left[G(T,p) - N_{Ti}\mu_{FeTiO_3} - \frac{1}{2}(N_{Fe} - N_{Ti})\mu_{Fe_2O_3}\right.$$
$$\left. + \frac{3}{2}(N_{Fe} + N_{Ti})\mu_O - N_O\mu_O\right] \quad (7)$$

As mentioned in the experimental procedure, the oxidation and reduction steps lasted for 30 minutes each and were alternated with an intermediate 10 minute flushing step using N_2 at

Fig. 6 $FeTiO_3$ (0001) surfaces and possible surface terminations.

11306 | *J. Mater. Chem. A*, 2015, **3**, 11302–11312

This journal is © The Royal Society of Chemistry 2015

100 mL min^{-1}. Therefore, it can be properly assumed that the surface is in a thermodynamic equilibrium state. Therefore, the chemical potential can be related to actual pressure and temperature conditions based on the thermodynamic equilibrium between the surface and the surrounding gas phase (assuming it is ideal gas) as:

$$\mu_O(T,p) = \frac{1}{2}\left[E_{O_2,\text{DFT}} + \mu^\circ_{O_2}(T,p^\circ) + k_B T \ln\left(\frac{p_{O_2}}{p^\circ}\right)\right] \quad (8)$$

According to present experimental methodology, the oxygen partial pressure was constant (200 mL min^{-1} flow of gas consisting of 50% air balanced with N$_2$, total 1 atm). Thus, the surface energies can be plotted as a function of oxygen chemical potential. The standard chemical potential $\mu^\circ_{O_2}(T,p^\circ)$ was taken from thermodynamic tables.[41] At 700 °C, the calculated surface energies are listed in Table 1.

From the surface energy calculation results, it can be seen that the Ti(1)–Ti(2)–O– terminated surface has the lowest surface energy 0.211 eV Å^{-2} and thus, it is the most stable FeTiO$_3$ particle surface structure in the oxidation step. The second most stable termination is Fe(1)–Fe(2)–O– with a surface energy of 0.257 eV Å^{-2}. Therefore, in chemical looping oxidation conditions, the Ti(1)–Ti(2)–O– structure is proposed as the dominant surface termination. This is shown in Fig. 7.

Initial relaxations of the Ti(1)–Ti(2)–O– surface from its cleaved bulk geometry led to a metastable geometry in which surface titanium atoms remained above the first oxygen layer. A displacement of one of the surface iron atoms into the cavity above the oxygen layer led to a less stable geometry with a higher energy. The relaxed top structure exhibits a tetrahedral configuration, where the O–Ti(1)–O angle is 79.8° and the O–Ti(2)–O angle is 103.5°. The Ti–O bonds are 2.095 Å for Ti(1) binding type and 1.833 Å for Ti(2) binding type, which both are slightly shorter than the Fe–O bonds with the lengths of 2.256 Å and 2.011 Å.

Oxygen adsorption and dissociation. Next, the adsorption of oxygen on FeTiO$_3$ (0001) surface with Ti(1)–Ti(2)–O– termination was studied. The O–O bond lengths of molecular oxygen are strongly correlated with the binding of O$_2$ to the surface due to the amount of electronic charge transferred to the molecule. On stoichiometric surfaces, two kinds of configurations were considered: O$_2$ adsorbed parallel to the surface (along either the x or y axis), and O$_2$ adsorbed perpendicular/vertical to the
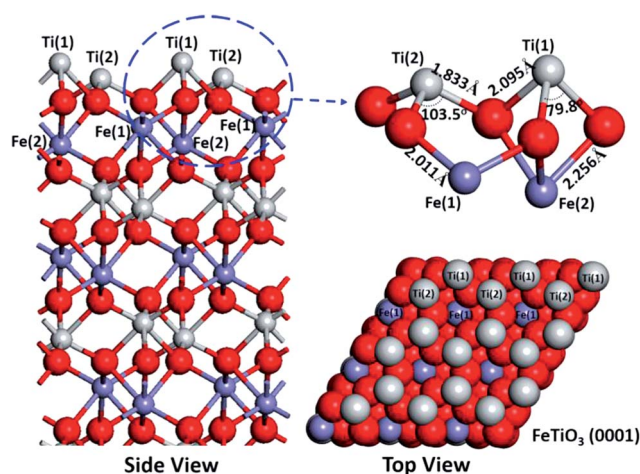

Fig. 7 Ti(1)–Ti(2)–O– terminated FeTiO$_3$ (0001) surface.

surface. The strongest energy of adsorption ($E_{\text{ads}} = -0.513$ eV) was observed for O$_2$ adsorbing as a "bridge" between two surface titanium atoms. Upon the adsorption, the O–Ti(1) bonds after relaxation were found to be slightly elongated to 2.112 Å while the O–Ti(2) bonds were slightly elongated to 1.875 Å. The calculated O–O bond length was 1.43 Å, which is larger than the value of the gas phase O$_2$ O–O bond of 1.23 Å. To compare the top surface metal ion activity, the O$_2$ adsorption on FeTiO$_3$ (0001) surface with Fe(1)–Fe(2)–O– termination also was investigated. Similarly, it was found O$_2$ bridging adsorption between two surface iron atoms is the most stable adsorption configuration ($E_{\text{ads}} = -0.385$ eV). However, the calculated length of O–O bond in adsorbed oxygen molecule was 1.31 Å, which is only slightly larger than the value of the gas phase O$_2$ O–O bond. It indicates stronger electron interaction between O$_2$ molecule and Ti ion than Fe ion.

The adsorption process itself results in a significant weakening of the O–O bonds of the oxygen molecule due to the elongation. Thus, it is essential to determine how these differences in structure, for both the Ti(1)–Ti(2)–O– termination and Fe(1)–Fe(2)–O– termination may dictate the reactivity of the system with respect to O$_2$ dissociation to form O ion.

The local minima and saddle points on the multi-dimensional potential energy surface were identified and optimized from the CI-NEB method. The computed O$_2$ dissociation energy profile is shown in Fig. 8. The total energy of O$_2$ molecule and clean FeTiO$_3$ (0001) surface is normalized to 0. The dissociation process initiated from the O$_2$ adsorption configuration (B and F in Fig. 8). Through the transition state, the O atoms in adsorbed oxygen molecule move toward atop site of Ti or Fe atom neighboring the surface oxygen atom, and overcome the energy barrier of 0.82 eV on Ti(1)–Ti(2)–O– terminated surface and 1.26 eV on Fe(1)–Fe(2)–O– terminated surface, to form two oxygen ions by breaking the O–O bond (D and H in Fig. 6). It is clearly seen that the Ti surface is more favorable for oxygen dissociation than the Fe surface. Therefore, the top Ti layer facilitates the oxygen dissociation to produce oxygen ion ready for transport into the surface.

Table 1 Surface energies of FeTiO$_3$ (0001) surface with various terminations at 700 °C (200 mL min^{-1} flow of gas consisting of 50% air balanced with N$_2$, total 1 atm)

Termination	Surface energy (eV Å^{-2})
(a) O–Fe(1)–Fe(2)–	0.362
(b) Fe(1)–Fe(2)–O–	0.257
(c) Fe(2)–O–Ti(1)–	0.335
(d) O–Ti(1)–Ti(2)–	0.402
(e) Ti(1)–Ti(2)–O–	0.211
(f) Ti(2)–O–Fe(1)–	0.319
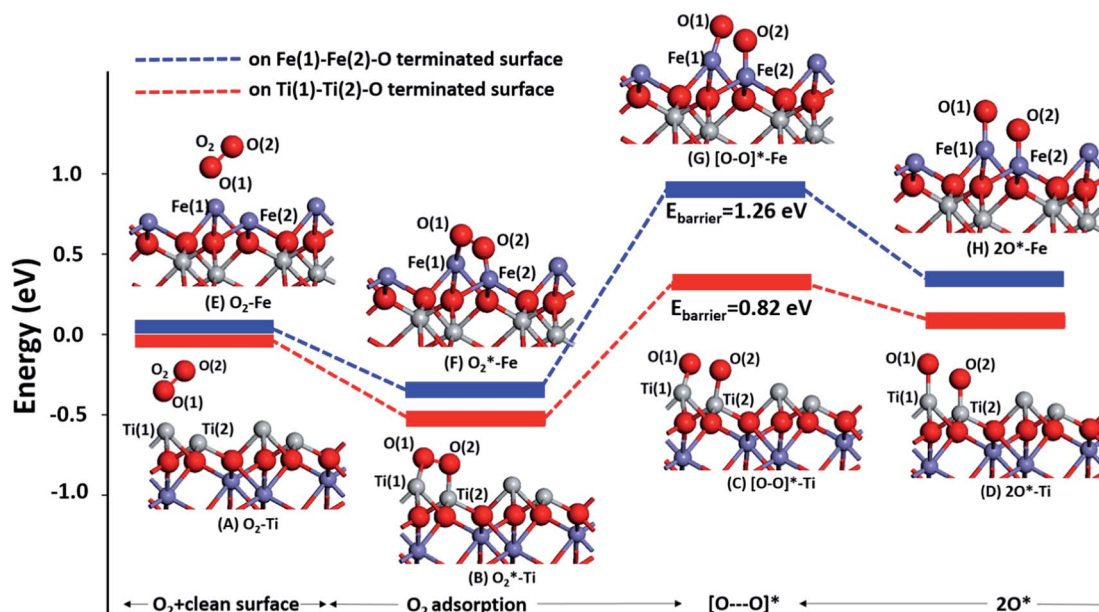
Fig. 8 Energy profile of O_2 dissociation on Ti(1)–Ti(2)–O– terminated $FeTiO_3$ (0001) surface and Fe(1)–Fe(2)–O– terminated $FeTiO_3$ (0001) surface.

Nanostructure growth and ion diffusion. The stress caused by the volume expansion during high temperature oxidation becomes a driving force for the nanostructure growth. When the grain/crystallite has a positive surface curvature, the outward diffusion of metal atoms serves as a continual source of ions for nanobelt growth and continues as long as the compressive stress in the metal oxide layer is maintained by volume expansion. Nanobelt will protrude perpendicularly to the grain surface due to the mechanical stress between neighboring grains.[42,43] The Ti and Fe ion diffusion was investigated further for deeper understanding of the nanobelt formation. No theoretical study has been carried out for the ion diffusion mechanism in $FeTiO_3$. Furthermore, no quantitative comparison has been made between Fe and Ti diffusion. In this study, we consider the most plausible pathways for Ti and Fe migration and evaluate their diffusion barriers which were calculated using CI-NEB. Stable positions of Fe or Ti ions corresponding to local energy minima are identified through atomic relaxation after a vacancy is introduced at the original site. The diffusion energy barrier is defined as the energy difference between the local minima and the transition state corresponding to the highest energy level along the Ti or Fe ion diffusion pathway. From subsurface to surface, five steps are chosen to describe the diffusion pathway which are labeled in Fig. 9. For step 1 in Ti diffusion, the transition state is located where Ti passes through a gap between two corner-sharing and one edge-sharing TiO_6 octahedrons. Here, Ti has a short bond length of about 1.65 Å with three neighboring O atoms and a diffusion energy barrier of 0.63 eV. Similar diffusion for Fe path is step 5. The transition state is located where Fe passes through a gap between two corner-sharing and one edge-sharing FeO_6 octahedrons. However, the Fe has a ~0.2 Å longer bond length with three neighboring O atoms and a 0.29 eV lower diffusion energy

barrier. The entire Ti diffusion and Fe diffusion energy profiles also are shown in Fig. 9. From the energy barrier diagram it was observed that the highest barrier for Fe ion diffusion is step 4 with 1.25 eV while the highest barrier for Ti ion diffusion is 0.66 eV. For step 4 in Ti diffusion, the transition state occurs at the edge of the edge-sharing octahedrons and Ti ions with low levels of energy are not expected to pass through it. In fact, except for step 3, the diffusion energy in all the other diffusion steps for Fe ions was found to be lower than Ti ions. This indicates that the outward diffusion of Fe ions is more favorable than Ti ions.

According to the diffusion rate equation,[44] diffusivity D is:

$$D = \varphi d^2 \exp\left(\frac{-E_a}{k_B T}\right) \tag{9}$$

where φ is the rate coefficient of hopping to a neighboring site, d is the migration distance, k_B is Boltzmann's constant and E_a is the energy barrier for the diffusion. According to Vineyard,[45] for a system containing N atoms, φ can be evaluated as:

$$\varphi = \frac{\prod_{i=1}^{3N} v_i^{\text{IN}}}{\prod_{j=1}^{3N-1} v_j^{\text{TS}}} \tag{10}$$

where v_i^{IN} and v_j^{TS} are the normal mode vibrational frequencies at the initial and transition state, respectively.

From equations above, the diffusivity of Fe ion was calculated to be 2.21×10^{-7} cm^2 s^{-1}, which matches reasonably well with that from a 2-D Fickian Continuum diffusion model[46] for Fe (1.3×10^{-7} cm^2 s^{-1}). The diffusivity of Ti ion was calculated to be 1.35×10^{-10} cm^2 s^{-1}. Therefore, Fe ion diffusivity is three orders of magnitude larger than Ti ion diffusivity, which serves to explain the formation of Fe_2O_3 nanobelt.
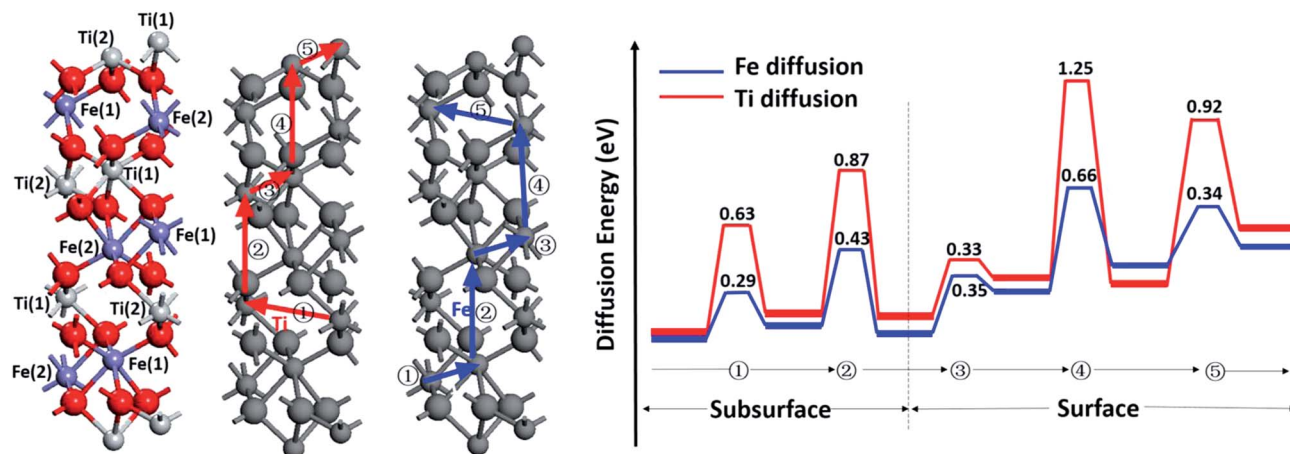
Fig. 9 Ti and Fe diffusion paths in FeTiO$_3$ (0001) surface and diffusion energy profile with energy barriers.

Thermal reduction of the oxidized microparticles in single and multiple redox cycles

The morphology evolution and mechanisms of vacancy formation of the Fe–Ti microparticles were further probed over single and multiple oxidation–reduction cycles, both at 700 and 900 °C. The morphological and structural changes observed upon single and five cycles and the oxygen vacancy formation calculations are discussed below.

Morphological and structural characterization upon reduction of Fe–Ti micropoarticles. The structure of the Fe–Ti microparticles was found to gradually changes over multiple redox cycles at 700 °C. The XRD spectra of the particles treated over one and five cycles can be seen in Fig. 1(c) and (d), respectively. The results show a phase change to Fe and TiO$_2$ upon reduction in both situations. The conversion to Fe and TiO$_2$ after five cycles is not complete as diffraction peaks from FeTiO$_3$ can be identified, showing that the reaction needs more time or higher temperatures to complete the transformation. Fig. 10(a) and (d) shows the SEM images of the surfaces of these Fe–Ti particles after one and five cycles, respectively.

The inset of Fig. 10(a) clearly shows a few partially retracted nanobelts. After five redox cycles, the nanobelts completely disappeared as shown in the inset of Fig. 10(d), which has been previously reported for other active metal oxide systems.[6] However, unlike the active metal oxide systems whose surfaces are highly dense due to unavoidable sintering effect,[6] in the present study it was discovered that the Fe–Ti microparticle surfaces become porous after redox cycles. This porous surface had not been observed for redox process of pure Fe microparticles.[6]

The porosity after five cycles was found to be higher than that after one cycle from BET measurement, the pore volumes in 1 and 5 cycled microparticle samples are comparable and the surface area in 1 and 5 cycled microparticle samples are 3.8 m^2 g^{-1} and 3.9 m^2 g^{-1}, respectively. This is consistent with SEM observation. This result suggests that the surface area of the Fe–Ti oxide system after redox cycles remain large despite sintering. This porous structures can be seen in Fig. 10 after redox treatment at 700 °C for both one and five cycles. Although

the original Fe–Ti microparticles were non-homogeneous, upon cyclic redox reactions the Fe and Ti were found to be uniformly distributed, as confirmed by the EDS analysis (Fig. 10(c) and (f)).

Similar to 700 °C, one and five redox cycles at 900 °C resulted in the formation of Fe and TiO$_2$ at the end of reduction. This was confirmed with their XRD spectrum in Fig. 4(b) and (c),
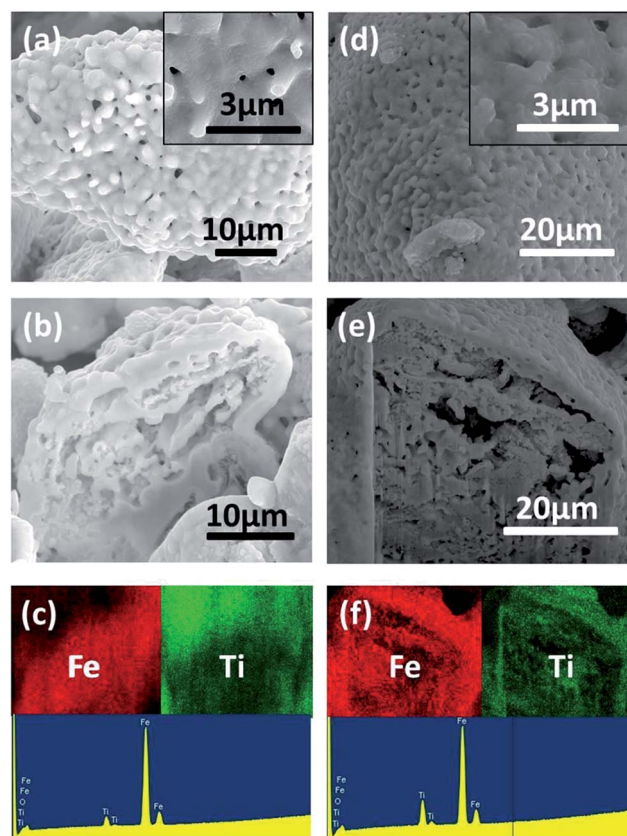

Fig. 10 Characterization of iron titanium microparticle at 700 °C. (a) SEM image of surface after one redox cycle, inset: higher magnification SEM image; (b) SEM image of cross section; and (c) EDS mapping and spectrum of (b); (d) SEM image of surface after five redox cycles, inset: higher magnification SEM image; (e) SEM image of cross section; and (f) EDS mapping and spectrum of (e) at 700 °C.

This journal is © The Royal Society of Chemistry 2015

J. Mater. Chem. A, 2015, **3**, 11302–11312 | **11309**

respectively. Fig. 11 shows the surface and cross sectional analysis of the samples treated at 900 °C. Micropores with a size of 1–3 μm were observed on the surface of the microparticles after one redox cycle. The surface porosity was observed to increase slightly after five redox cycles (Fig. 11(d) and (e)), which is consistent with 700 °C results. Comparing Fig. 10(d) and 11(d), the porosity was found to be clearly higher for microparticles treated at 900 °C.

In a previous work,[6] it was demonstrated that a severe sintering effect hinders active metals or alloys from being used effectively in high temperature applications including chemical looping processes. In this work, it is proven that the addition of inert oxides, which is defined as metal oxides with negligible reaction rates with reducing or oxidizing gases, is able to offset the sintering effects by creating micropores on the microparticle surfaces.

Computation of oxygen vacancy formation during reduction. In the reduction step for the present Fe–Ti system, oxygen is released to the gas phase and oxygen vacancy is formed. The formation energy of the vacancy is determined as follows:

$$E(V_O^{\cdot\cdot}) = E(FeTiO_3, V_O^{\cdot\cdot}) - E(FeTiO_3) + \frac{1}{2}E(O_2) \quad (11)$$

where $E(FeTiO_3)$ is the energy of $FeTiO_3$, $E(FeTiO_3, V_O^{\cdot\cdot})$ is the energy of $FeTiO_3$ with a vacancy, and $E(O_2)$ is the energy of molecular oxygen.

By replacing the energy of oxygen molecule in the vacancy formation equation by the oxygen chemical potential, the vacancy formation energies at temperatures relevant to chemical looping were calculated by:

$$\Delta G(V_O^{\cdot\cdot}) = E(FeTiO_3, V_O^{\cdot\cdot}) - E(FeTiO_3) + \frac{1}{2}\mu_O(T,p) \quad (12)$$

These vacancies are created at the $FeTiO_3$ surface and on the $FeTiO_3$ subsurface by removing the oxygen atom as shown in Fig. 12. H atoms are located on atop site of surface Ti atoms in this reduction process for more accurate calculations.

As mentioned above, the porous surface had not been observed for Fe_2O_3 reduction process at the same redox condition; a Fe_2O_3 surface is thus modelled for comparisons. Among the iron oxides, corundum-type α-Fe_2O_3 is the most thermodynamically stable form of iron oxide under our experimental conditions.[47] The α-Fe_2O_3 structure contains iron and oxygen atoms arranged in a trigonal-hexagonal structure with space group $R\overline{3}c$. The arrangement of the cations produces pairs of FeO_6 octahedra that share edges with three neighboring octahedra in the same plane and one face with an octahedron in an adjacent plane in the [001] direction. The Fe_2O_3 (0001) surfaces of natural α-Fe_2O_3 have been shown to be the dominant growth faces.[48] Detailed structural characterization of the Fe_2O_3 (0001) surface revealed that surface termination depends on different conditions of temperature and oxygen partial pressure.[49,50] Theoretical calculations by
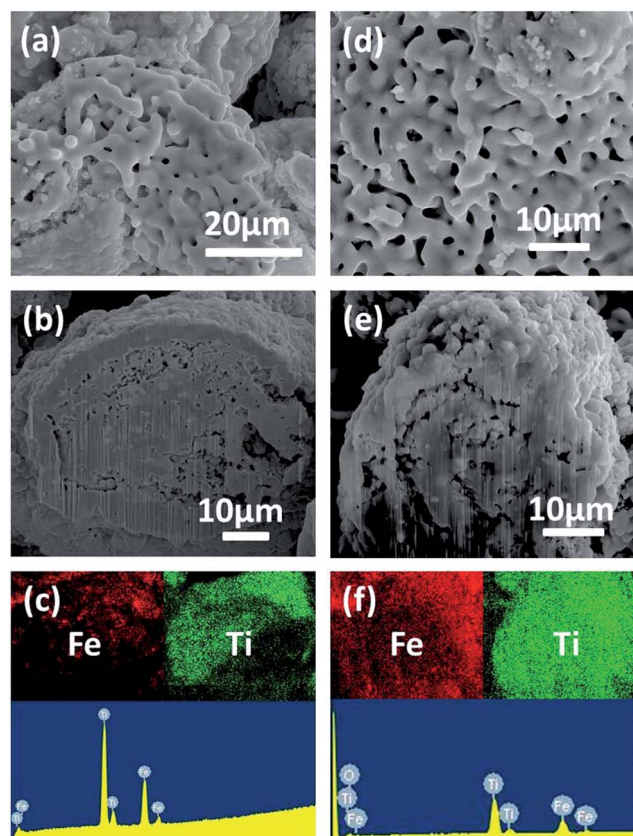

Fig. 11 Characterization of iron titanium microparticle at 900 °C. (a) SEM image of surface after one redox cycle; (b) SEM image of cross section; and (c) EDS mapping and spectrum of (b); (d) SEM image of surface after five redox cycles; (e) SEM image of cross section; and (f) EDS mapping and spectrum of (e).
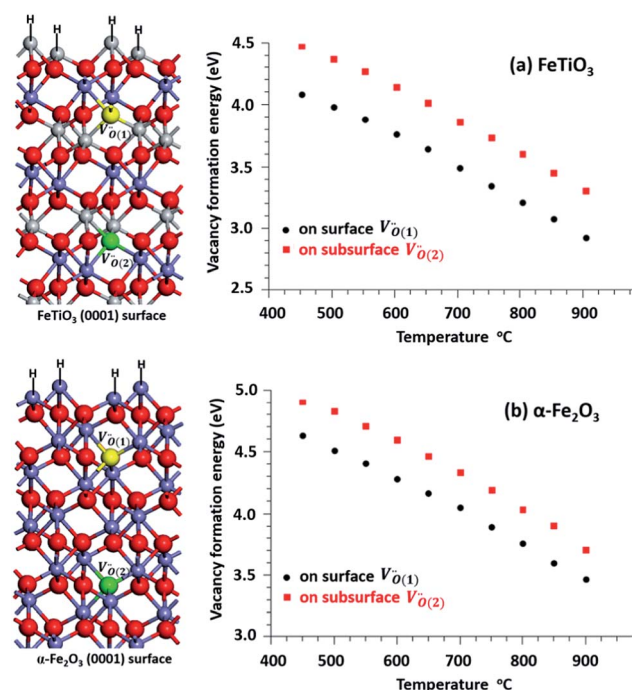

Fig. 12 Vacancy formation energy on the surface and on the subsurface as a function of temperature at pressure 1 atm for (a) $FeTiO_3$ and (b) α-Fe_2O_3 phases. Yellow ball represents the surface vacancy $V_{O(1)}^{\cdot\cdot}$ and green ball represents the subsurface vacancy $V_{O(2)}^{\cdot\cdot}$.

11310 | *J. Mater. Chem. A*, 2015, **3**, 11302–11312

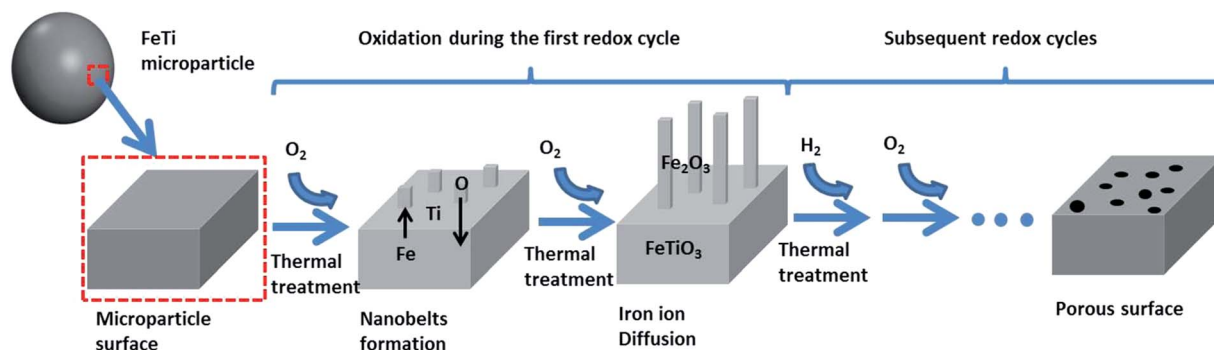This journal is © The Royal Society of Chemistry 2015

Fig. 13 Schematic illustration of Fe–Ti microparticles and their oxidation and redox processes.

Trainor *et al.*[51] and Wang *et al.*[47] showed that the Fe$_2$O$_3$ (0001) surface can be terminated by either a single or double Fe layer or by oxygen ions, although the unreconstructed double Fe-termination and oxygen-terminated surface are dipolar. In our experimental condition, double Fe layer termination is found to be the most stable with lowest surface energy of 0.277 eV Å^{-2}.

Based on eqn (12), the relationship between the temperature and the vacancy formation energies is presented in Fig. 12 (right) for FeTiO$_3$ and Fe$_2$O$_3$ phases. It is seen that when the temperature increases, the vacancy formation energy decreases. The vacancy formation on the surface was found to be thermodynamically more favorable than vacancy formation on the subsurface. Compared with Fe$_2$O$_3$, the vacancy formation energy on FeTiO$_3$ was seen to be about 0.5 eV lower. This result indicates that the formation of oxygen vacancies ($V_O^{\cdot\cdot}$) through the outward diffusion of oxygen ions (O^{2-}) during the reduction reaction to form the porous surface is easier on FeTiO$_3$ particle than on Fe$_2$O$_3$ particle. This finding can explain the experimental result in which there was a porous structure on FeTiO$_3$ surface in the reduction step while no pore was seen on the Fe$_2$O$_3$ surface in the same condition.

The oxidation and redox processes are illustrated in Fig. 13. To better describe the evolution process, an infinitesimal element of the microparticle at 700 °C was selected as indicated by the red dotted frame. The surface of this element can be approximated to be flat. The driving force of the protrusion is volume expansion. The diffusion of Fe ions was found to be faster than the Ti ions. Consequently, the nanobelts were proved mainly to be Fe$_2$O$_3$ with Ti remaining in the microparticles. The reduction causes oxygen vacancy generation in FeTiO$_3$ phase which is substantially easier than in Fe$_2$O$_3$. The vacancy induced pore formation explains the superior recyclability of Fe–Ti microparticles over pure Fe microparticles.

Conclusions

The iron–titanium based oxide composites, which can be used as enabling materials in energy conversion systems, can greatly improve the reactivity of iron oxides alone over multiple redox cycles in chemical looping applications. The nanostructure formation and reaction mechanism for the microparticle of these composite materials are examined in this study. The Fe–Ti was found to transform to mixed phases containing FeTiO$_3$ and TiO$_2$ after oxidation at both 700 °C and 900 °C while unreacted Fe was found at 700 °C rather than 900 °C due to complete reactions at the higher temperature. Thermal oxidation at 700 °C resulted in the formation of nanobelts on the microparticle surface. Atomistic thermodynamics methods and DFT calculations were used to probe the surface nanostructure stability and the relationship between FeTiO$_3$ surface termination and the temperature/pressure. It was found that Ti–Ti–O–terminated surface is the most stable surface with the lowest surface energy under the redox conditions. The O$_2$ adsorption occurs on two surface Ti sites and the follow-up dissociation produces two oxygen ions with energy barrier of 0.82 eV which is 0.44 eV lower than the adsorption energy barrier on the Fe–Fe–O–terminated surface, indicating that threefold Ti top layer facilitates the oxygen ions formation. However, Ti ion diffusion on FeTiO$_3$ was found to be slower than Fe ion due to higher diffusion barrier, therefore the outward diffusion of Fe ions are oxidized to form iron oxide nanobelts with the stress driving force while Ti remaining in FeTiO$_3$ particle. In the reduction process, these Fe–Ti composite materials are transformed to mixed phases of Fe and TiO$_2$ after one or multiple redox cycles at both 700 °C and 900 °C. The oxygen vacancy formation energy of FeTiO$_3$ was found to decrease with the increasing temperature; however it was about 0.5 eV lower than Fe$_2$O$_3$, which indicates that it is easier to form defective surface structures on FeTiO$_3$ in the redox process. This finding is in good agreement with experimental results in which the porous structure formed on the FeTiO$_3$ surface in the reduction step while little pore-formation was found on Fe$_2$O$_3$ surface under the same reaction condition. Further, the microblades were found to form on the microparticle surface at 900 °C due to the sintering effect and also the microparticle became highly porous due to the oxygen defects clustering during the reduction process. This observation explains the excellent recyclability of iron titanium oxide particles in the applications that involve cyclic ionic transport. The fundamental insight into the mechanism of cyclic redox reactions of Fe–Ti microparticles at the nanoscale revealed in this study can be applied to other active-inert metal oxide systems used in a wide variety of chemical looping applications.

Acknowledgements

Notes and references

1 M. Law, L. Greene, J. Johnson, R. Saykally and P. Yang, *Nat. Mater.*, 2005, **4**, 455.

2 A. Hauch, S. D. Ebbesen, S. H. Jensen and M. Mogensen, *J. Mater. Chem.*, 2008, **18**, 2331.

3 X. Xu, C. Randorn, P. Efstathiou and J. Irvine, *Nat. Mater.*, 2012, **11**, 595.

4 L.-S. Fan, L. Zeng, W. Wang and S. Luo, *Energy Environ. Sci.*, 2012, **5**, 7254.

5 P. M. Rao and X. Zheng, *Nano Lett.*, 2009, **9**, 3001.

6 L. Qin, A. Majumder, J. A. Fan, D. Kopechek and L.-S. Fan, *J. Mater. Chem. A*, 2014, **2**, 17511.

7 X. Liu, C. Lee, C. Zhou and J. Han, *Appl. Phys. Lett.*, 2001, **79**, 3329.

8 J. Barrelet, A. B. Greytak and C. M. Lieber, *Nano Lett.*, 2004, **4**, 1981.

9 J. Wang, X. An, Q. Li and R. F. Egerton, *Appl. Phys. Lett.*, 2005, **86**, 201911.

10 B. Wei, K. Zheng, Y. Ji, Y. Zhang, Z. Zhang and X. Han, *Nano Lett.*, 2012, **12**, 4595.

11 L.-S. Fan and F. Li, *Ind. Eng. Chem. Res.*, 2010, **49**, 10200.

12 D. D. Figueroa, T. Fout, S. Plasynski, H. McIlvried and R. D. Srivastava, *Int. J. Greenhouse Gas Control*, 2008, **2**, 9.

13 A. Lyngfelt, *Oil Gas Sci. Technol.*, 2011, **66**, 161.

14 L. Zeng, S. Luo, D. Sridhar and L.-S. Fan, *Rev. Chem. Eng.*, 2012, **28**, 1.

15 J. Adánez, L. F. de Diego, F. García-Labiano, P. Gayán and A. Abad, *Energy Fuels*, 2004, **18**, 371.

16 T. Mattisson, H. Leion and A. Lyngfelt, *Fuel*, 2009, **88**, 683.

17 F. Li, H. R. Kim, D. Sridhar, F. Wang, L. Zeng, J. Chen and L.-S. Fan, *Energy Fuels*, 2009, **23**, 4182.

18 Q. Song, R. Xiao, Z. Deng, W. Zheng, L. Shen and J. Xiao, *Energy Fuels*, 2008, **22**, 3661.

19 F. Li, Z. Sun, S. Luo and L.-S. Fan, *Energy Environ. Sci.*, 2011, **4**, 876.

20 G. Kresse and J. Hafner, *Phys. Rev. B: Condens. Matter Mater. Phys.*, 1993, **47**, 558.

21 G. Kresse and J. Furthmuller, *Comput. Mater. Sci.*, 1996, **6**, 15.

22 G. Kresse and J. Furthmuller, *Phys. Rev. B: Condens. Matter Mater. Phys.*, 1996, **54**, 11169.

23 J. P. Perdew, K. Burke and M. Ernzerhof, *Phys. Rev. Lett.*, 1996, **77**, 3865.

24 P. E. Blöchl, *Phys. Rev. B: Condens. Matter Mater. Phys.*, 1994, **50**, 17953.

25 G. Kresse and D. Joubert, *Phys. Rev. B: Condens. Matter Mater. Phys.*, 1999, **59**, 1758.

26 P. E. Blöchl, O. Jepsen and O. K. Anderson, *Phys. Rev. B: Condens. Matter Mater. Phys.*, 1994, **49**, 16223.

27 J. F. Herbst, R. E. Watson and J. W. Wilkins, *Phys. Rev. B: Condens. Matter Mater. Phys.*, 1978, **17**, 3089.

28 V. I. Anisimov and O. Gunnarsson, *Phys. Rev. B: Condens. Matter Mater. Phys.*, 1991, **43**, 7570.

29 B. A. Wechsler and C. T. Prewitt, *Am. Mineral.*, 1984, **69**, 176.

30 H. Jónsson, G. Mills and K. W. Jacobsen, in *Classical and Quantum Dynamics in Condensed Phase Simulations*, ed. B. J. Berne, G. Ciccotti and D. F. Coker, World Scientific, 1998, p. 385.

31 G. Henkelman, B. P. Uberuaga and H. J. Jonsson, *J. Chem. Phys.*, 2000, **113**, 9901.

32 P. Uberuaga and X.-M. Bai, *J. Phys.: Condens. Matter*, 2011, **23**, 435004.

33 Y. Fu, J. Chen and H. Zhang, *Chem. Phys. Lett.*, 2001, **350**, 491.

34 X. Wen, S. Wang, Y. Ding, Z. L. Wang and S. Yang, *J. Phys. Chem. B*, 2005, **109**, 215.

35 M. Farbod, N. M. Ghaffari and I. Kazeminezhad, *Ceram. Int.*, 2014, **40**, 517.

36 H. Y. Dang, J. Wang and S. S. Fan, *Nanotechnology*, 2003, **14**, 738.

37 X. Wen, S. Wang, Y. Ding, Z. L. Wang and S. Yang, *J. Phys. Chem. B*, 2005, **109**, 215.

38 J. Huang, Z. Huang, S. Yi, Y. Liu, M. Fang and S. Zhang, *Sci. Rep.*, 2013, **3**, 3504.

39 N. C. Wilson, J. Muscat, D. Mkhonto, P. E. Ngoepe and N. M. Harrison, *Phys. Rev. B: Condens. Matter*, 2005, **71**, 075202.

40 R. A. Fellows, A. R. Lennie, D. J. Vaughan and G. Thornton, *Surf. Sci.*, 1997, **383**, 50.

41 M. W. Chase, C. Daveis, J. Downey, D. J. Furip, R. A. McDonald and A. N. Syverud, *JANAF Thermochemical Tables*, US National Bureau of Standards, Washington, DC, 3rd edn, 1985.

42 M. Goncalves, L. C. Campos, A. S. Ferlauto and R. G. Lacerda, *J. Appl. Phys.*, 2009, **106**, 034303.

43 A. Kumar, A. K. Srivastava, P. Tiwari and R. V. Nandedkar, *J. Phys.: Condens. Matter*, 2004, **16**, 8531.

44 N. Peterson, *J. Nucl. Mater.*, 1978, **69**, 3.

45 G. H. Vineyard, *J. Phys. Chem. Solids*, 1957, **3**, 121.

46 Z. Sun, Q. Zhou and L.-S. Fan, *Langmuir*, 2012, **28**, 11827.

47 X. G. Wang, W. Weiss, S. K. Shaikhutdinov, M. Ritter, M. Petersen, F. Wagner, R. Schlögl and M. Scheffler, *Phys. Rev. Lett.*, 1998, **81**, 1038.

48 R. M. Cornell and U. Schwertmann, *The Iron Oxides: Structure, Properties, Reactions, Occurrences and Uses*, Wiley-VCH, New York, 2nd edn, 2003.

49 S. K. Shaikhutdinov and W. Weiss, *Surf. Sci.*, 1999, **432**, L627.

50 S. A. Chambers and S. I. Yi, *Surf. Sci.*, 1999, **439**, L785.

51 T. P. Trainor, A. M. Chaka, P. J. Eng, M. Newville, G. A. Waychunas, J. G. Catalano and G. E. Brown Jr, *Surf. Sci.*, 2004, **573**, 204.